Plasmonic enhancement of the magneto-optical response of MnP nanoclusters embedded in GaP epilayers

Gabriel Monette, Nima Nateghi, Remo A. Masut, Sébastien Francoeur,[*] and David Ménard

Regroupement Québécois sur les Matériaux de Pointe (RQMP), Département de Génie Physique,
École Polytechnique de Montréal, C.P. 6079, succ. Centre-ville, Montréal, Québec, Canada H3C 3A7

We report on the magneto-optical activity of MnP nanoclusters embedded in GaP epilayers and MnP thin film as a function of temperature, magnetic field, and wavelength in the near infrared and visible. The measured Faraday rotation originates from the ferromagnetic magnetization of the metallic MnP phase and exhibits a hysteretic behavior as a function of an externally applied magnetic field closely matching that of the magnetization. The Faraday rotation spectrum of MnP shows a magnetoplasmonic resonance whose energy depends on the MnP filling factor and surrounding matrix permittivity. At resonance, the measured rotary power for the epilayer systems increases by a factor of 2 compared to that of the MnP film in terms of degrees of rotation per MnP thickness for an applied magnetic field of 410 mT. We propose an effective medium model, which qualitatively reproduces the Faraday rotation and the magnetocircular dichroism spectra, quantitatively determines the spectral shift induced by variations in the MnP volume fraction, and demonstrates the influence of the shape and orientation distributions of ellipsoidal MnP nanoclusters on the magneto-optical activity and absorption spectra.

I. INTRODUCTION

Magnetoplasmonic materials continue to attract considerable attention for their potential applications in optoelectronic and biomedical technologies.[1,2] Materials most commonly studied include noble-metal particles embedded in magnetic hosts,[3] core-shell assembled magnetic-metal materials,[4] or multilayer arrangements containing alternating metallic films and magnetic layers.[5,6] In these systems, the magnetoplasmonic coupling takes place at the boundary between the plasmon supporting metal and the magnetic material.[7]

Another approach to achieve a significant magnetoplasmonic coupling consists in embedding magnetic metallic inclusions in a dielectric host. In this less studied approach,[8] the contribution of free electrons to the permittivity of small metallic spheres leads to a dielectric polarizability, similar in form to that of the electronic polarizability of atoms, with a characteristic resonance usually found in the ultraviolet. For metallic spheres embedded in a dielectric host, this plasmonic resonance is expected to shift to lower frequencies. Indeed, a Maxwell-Garnett model reveals that it is in direct relation to the permittivity contrast of both constituents and to the volume fraction of metallic spheres. Unlike surface plasmons, this mechanism involves a resonant enhancement of the oscillations of the degenerate electron gas throughout the volume, which is accompanied by a corresponding enhancement of its magnetoactive response. With proper choice of magnetoactive material and host matrix permittivity, resonant magneto-optical (MO) effects can then be tuned to match that of technologically relevant wavelengths for applications. In this context, semiconductor hosts are prime candidates for their integration with current electronic and optoelectronic technologies.

In this work, we investigate the magneto-optical properties of manganese phosphide (MnP) nanoclusters embedded in gallium phosphide (GaP). This GaP:MnP system, which serves as a prototype of similar systems, such as GaAs:MnAs, is particularly interesting for a number of reasons. First, the intrinsically large spin-orbit coupling of MnP promotes the presence of strong first-order magneto-optical effects such as Faraday rotation[9] and a variety of higher order effects such as magnetostriction and magnetocaloric effects.[10] This magnetic material therefore offers advantageous characteristics for the design of novel sensors and other applications. Second, the GaP matrix offers two important advantages: Its relatively large energy band gap provides a wide transparency window in the visible and its lattice parameter matches that of silicon for ease of integration with current semiconductor technology.

This paper is organized as follows. The next section presents the GaP:MnP material system and describes the important characteristics of the samples studied in this work. Section III presents the effective medium model developed to interpret and model the experimental magneto-optical data. The following sections then present the Faraday rotation and magnetocircular dichroism as a function of the applied magnetic field, temperature, and probing photon energy. Using various figures of merit, we then evaluate and compare the amplitude of the optical activity and discuss the limitations imposed by the broad distributions of nanocluster shapes and orientations. We conclude that present epilayer samples do increase the magneto-optical activity when compared to MnP thin film but that better homogenization of the embedded MnP nanoclusters during the growth process is required to optimize the observed magnetoplasmonic resonant behavior.

II. SAMPLES AND STRUCTURAL CHARACTERIZATION

All samples shown in Table I, except D1, were grown using metal-organic vapor phase epitaxy (MOVPE) from precursors and under conditions described in Ref. 11. Sample A1 is a MnP film fabricated to investigate the magneto-optical response of MnP, for which we found no data in the literature. The film was deposited on glass and has a thickness, evaluated from thicker films grown under identical

TABLE I. Sample descriptions.

Sample	Composition; Thickness	Substrate	Volume fraction	Effective magnetic anisotropy	Cluster size (nm)
A1	MnP film; 100 nm	Glass	100%	Easy plane	
B1–B4	GaP:MnP; 650, 900, 1500, 2000 nm	GaP (011)	3.8%	Easy axis along GaP $\langle 011 \rangle$	12–36
C1	GaP:MnP; 830 nm	GaP (001)	13.7%	Easy axis along GaP $\langle 011 \rangle$	26–36
D1	Ps:MnP; $\approx 140\ \mu$m		$\leqslant 1\%$	None	10–80

conditions, of about 100 nm. It shows a mirror-like surface and scanning electron microscopy (SEM) reveals a polycrystalline structure with an average in-plane grain diameter of 150 nm. Angular-dependent magnetization measurements using vibrating sample magnetometry (VSM) indicate an easy plane of magnetization (coplanar to the plane of the sample), dominated by the shape anisotropy induced demagnetization field.

Epilayers of GaP with embedded nanoclusters of MnP (GaP:MnP) were grown under two different sets of conditions, for which the fabrication technique and subsequent characterization follow the same approach as described in Ref. 11. Samples from set B were grown on 400 μm GaP (011) with thicknesses of 650, 900, 1500, and 2000 nm (samples B1 to B4, respectively). For this set of samples, cross-sectional transmission electron microscopy (TEM) studies reveal the presence of MnP clusters with a diameter distribution ranging from 12 to 36 nm and occupying 3.8% of the epilayer volume. MnP nanoclusters are well contrasted relative to the surrounding matrix, which does not exhibit apparent defects. Sample C1, grown on 500 μm GaP (001), has a thickness of 830 nm. TEM micrographs reveal a cluster diameter distribution ranging from 26 to 36 nm and a volume occupancy of 13.7%. As has already been reported, samples B and C are magnetically textured, with the easy magnetocrystalline c axis of the MnP clusters mainly oriented along the GaP $\langle 011 \rangle$ families of directions.[11,12] Low-temperature properties and magnetic phase diagrams in these systems have also been recently investigated,[13] showing a distinct behavior compared to that of bulk MnP. Those studies revealed that the GaP:MnP epilayers have a slightly higher Curie temperature (T_c) than that of bulk MnP (297–305 K compared to 291.5 K[14]). For all heterogeneous epilayers (samples from set B and C), TEM micrographs similar to those reported in Ref. 11 show that the MnP nanoparticles have a relatively important distribution of eccentricities, for which mean diameters were extracted and summarized in Table I.

Sample D1 consists of MnP nanoclusters laser ablated from bulk MnP crystal and embedded into a polystyrene matrix (Ps:MnP). These were made to study the effect of the matrix surrounding the MnP clusters on the magneto-optical properties. The MnP nanoclusters occupy less than 1% of the volume and the thickness of the polystyrene film is about 140 μm. TEM micrographs reveal a unimodal diameter distribution ranging from 10 to 80 nm, but nearly spherical shapes (average long over short axis ratio of 1.07). Table I summarizes the principal characteristics of the samples studied in this article.

III. MAGNETO-OPTICAL RESPONSE

In this section, an effective medium model is developed to gain a better understanding of the physics at play in this heterogeneous system. Epitaxial GaP:MnP films are assumed to behave as an effective medium based on their two constituents: the metallic ferromagnetic clusters and the semiconducting matrix. The effective medium permittivity is obtained from Maxwell-Garnett mixing rules, for which the metal is treated as a degenerate free electron gas subjected to a magnetization-dependent effective internal magnetic field and the semiconducting matrix is considered as an isotropic dielectric. This effective medium permittivity is known to present a resonant behavior, which is referred to as the magnetoplasmonic resonance of the system for two reasons: First, it originates from the shift of the plasmonic frequency of the constituent metal inclusions as a function of the mixing filling factor and of the permittivity contrast between the matrix and the inclusions. Second, the effective medium permittivity possesses a magnetic dependence in the off-diagonal tensor elements, indicative of magneto-optical activity.

The spectral dependence of the free carrier contribution to the permittivity tensor components can be obtained from Boltzmann formalism[15] and eventually extended by taking into account the interband electronic transitions. For a degenerate free electron gas, neglecting spatial dispersion and assuming a relaxation time approximation, a one-electron Drude model essentially accounts for the magnetic field and frequency dependent behavior of the permittivity tensor.[15] At optical frequencies, the permittivity tensor of the metallic clusters, with a magnetic field parallel to the propagation of the light, is given by (see Appendix A)

$$
\overleftrightarrow{\epsilon_i} = \epsilon_0 \begin{pmatrix} 1 - \frac{\omega_p^2}{(\omega^2 + i\omega\gamma)} & -i\frac{-\omega\omega_c\omega_p^2}{(\omega^2 + i\omega\gamma)^2} & 0 \\ i\frac{-\omega\omega_c\omega_p^2}{(\omega^2 + i\omega\gamma)^2} & 1 - \frac{\omega_p^2}{(\omega^2 + i\omega\gamma)} & 0 \\ 0 & 0 & 1 - \frac{\omega_p^2}{(\omega^2 + i\omega\gamma)} \end{pmatrix}. \quad (1)
$$

In this expression, ϵ_0 is the free-space permittivity, ω is the incident light angular frequency, $\omega_p = (\frac{n_e e^2}{m^* \epsilon_0})^{1/2}$ is the plasma angular frequency, n_e is the electronic density, e is the electronic charge and m^* is the electron effective mass, γ is a damping parameter corresponding to the inverse of the Drude relaxation time, and $\omega_c = \frac{eB}{m^*}$ is the electron cyclotron angular frequency, where B is the induction field, including the applied field as well as a Weiss-like effective field in the form λM, where λ is the effective MO coupling parameter and M the sample magnetization.

The permittivity of the zinc-blende GaP matrix is considered as an isotropic scalar quantity independent of frequency for $\hbar\omega$ below the semiconductor energy gap. Its gyrotropic off-diagonal contribution to the effective medium response is not significant and can be ignored for the mixing rules. The increase of the imaginary and real parts for energies near and above the semiconductor gap could lead to slight variations in the effective permittivity tensor obtained from the mixing rules, but these are not expected to dominate the line shape, which is mostly defined by the plasmonic shift in the investigated spectral window.

For energies below the GaP semiconductor gap, the Maxwell-Garnett approach for an effective medium made of randomly oriented ellipsoidal metallic inclusions with varying shapes and of permittivity $\overleftrightarrow{\epsilon_i}$ in a surrounding matrix of scalar permittivity ϵ_m gives an effective permittivity tensor $\overleftrightarrow{\epsilon}_{\text{eff}}$ expressed as (see Appendix B)

$$\overleftrightarrow{\epsilon}_{\text{eff}} = \epsilon_m \overleftrightarrow{I} + \left[\overleftrightarrow{I} - \frac{n_i}{\epsilon_m} \sum_k \rho_k \int_\Omega d\Omega \, \overleftrightarrow{\alpha_k}(\Omega) \cdot \overleftrightarrow{N_k}(\Omega) \right]^{-1}$$

$$\cdot \, n_i \sum_k \rho_k \int_\Omega d\Omega \, \overleftrightarrow{\alpha_k}(\Omega)$$

$$\equiv \begin{pmatrix} \epsilon_{\text{eff},\perp} & -i\epsilon_{\text{eff,t}} & 0 \\ i\epsilon_{\text{eff,t}} & \epsilon_{\text{eff},\perp} & 0 \\ 0 & 0 & \epsilon_{\text{eff},\parallel} \end{pmatrix}, \qquad (2)$$

where $\overleftrightarrow{I}$ is the identity tensor, n_i is the number density of inclusions, $\overleftrightarrow{N_k}$ is the shape factor depolarization tensor of the inclusion population ellipsoids, and $\overleftrightarrow{\alpha_k}$ is the polarizability tensor of that same population of inclusions, characterized by the permittivity given by Eq. (1) (see Appendix A). The sum over k and weight function ρ_k are used to model an ensemble of inclusions with varying shapes and orientations (Ω) with respect to the gyrotropic axis.

The Faraday rotation corresponds to the rotation of the polarization plane of the incident light induced in the medium by a specific applied magnetic field and the corresponding magnetization state. For propagation along the applied and magnetization fields, this angle per unit length (rad m^{-1}) is expressed as[16]

$$\Phi_F = \frac{\omega\sqrt{\mu_0}}{2} [\sqrt{(\epsilon_{\text{eff},+})} - \sqrt{(\epsilon_{\text{eff},-})}], \qquad (3)$$

where the circular effective permittivities are defined as $\epsilon_{\text{eff},\pm} = \epsilon_{\text{eff},\perp} \pm \epsilon_{\text{eff,t}}$. Since $\epsilon_{\text{eff},\perp} \gg \epsilon_{\text{eff,t}}$, the Faraday rotation angle per unit of length is reduced to

$$\Phi_F \approx \frac{\omega\sqrt{\mu_0}}{2} \frac{\epsilon_{\text{eff,t}}}{\sqrt{\epsilon_{\text{eff},\perp}}}, \qquad (4)$$

where the real part of this equation yields the actual rotation of the polarization, while the imaginary part yields the magnetocircular dichroism (MCD).

For perfectly spherical inclusions, $\epsilon_{\text{eff,t}}$ and $\epsilon_{\text{eff},\perp}$ share the same denominator and the effective resonant frequency for both components reduces to

$$\omega_{\text{res}} = \frac{\omega_p}{\left[1 + \frac{(2+f)}{(1-f)} \frac{\epsilon_m}{\epsilon_0} \right]^{1/2}}. \qquad (5)$$
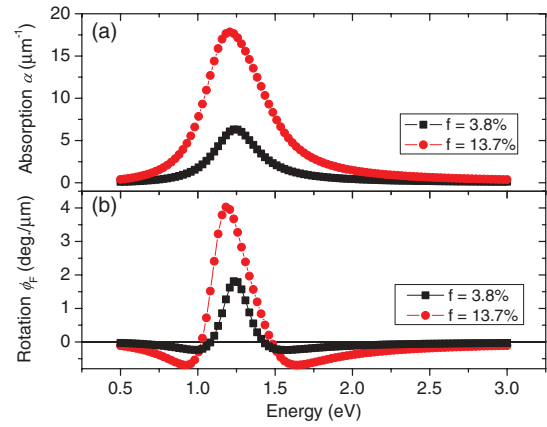

FIG. 1. (Color online) (a) Absorption spectra evaluated from effective permittivity components for a mixture of metallic MnP spheres embedded in a matrix of GaP with inclusion volume fractions of 3.8% and 13.7%. The Lorentz-type resonance in the effective permittivity redshifts the absorption maximum when increasing the volume filling factor. (b) Magneto-optical Faraday rotation spectra for the same systems. The enhanced Faraday rotation derives from the resonance in effective permittivity and an effective internal magnetic field of $\lambda M = 15$ T.

This shows a Lorentz-type resonance at an effective plasma frequency related to the permittivity of the matrix, ϵ_m, and volume filling factor, f. This resonance is seen in both the diagonal and off-diagonal elements of the effective permittivity tensor and governs the absorption and optical activity spectra, respectively. This result is similar to that presented in Ref. 8 in the context of Kerr effect measurements.

Figure 1 shows the calculated absorption $\alpha(\omega) = \omega\sqrt{\mu_0}\sqrt{\frac{\sqrt{\epsilon_{\text{eff},\perp}'^2 + \epsilon_{\text{eff},\perp}''^2} - \epsilon_{\text{eff},\perp}'}{2}}$, where $\epsilon_{\text{eff},\perp}' = \text{Re}[\epsilon_{\text{eff},\perp}]$ and $\epsilon_{\text{eff},\perp}'' = \text{Im}[\epsilon_{\text{eff},\perp}]$, and the Faraday rotation angle per unit length $\phi_F = \text{Re}[\frac{180}{\pi}\Phi_F] = \text{Re}[\frac{180}{\pi}\frac{\omega\sqrt{\mu_0}}{2}\frac{\epsilon_{\text{eff,t}}}{\sqrt{\epsilon_{\text{eff},\perp}}}]$ of spherical inclusions of MnP in GaP at the two filling factors relevant to this study, 3.8% and 13.7%. For this calculation, a plasma frequency of 6.0 eV (calculated from the resistivity reported in Ref. 17), a permittivity ϵ_m of $11\epsilon_0$, an effective internal MO coupling field λM of 15 T, and a relaxation parameter $1/\tau = \gamma = 5 \times 10^{14}$ rad s^{-1} were used. While the plasma frequency of MnP is similar to that of other Mn pnictides,[18] it is important to note that the MO properties of MnP are not well known, leading to some uncertainty on those parameters. The spectra of Fig. 1 indicate that the magnetoplasmonic resonance is located in the near infrared at around 1.25 eV, an energy mostly dominated by ω_p and ϵ_m/ϵ_0 and with a slight dependance on the filling factor. It is important to note that the width of the resonance is rather broad, even for an ensemble of identical spherical inclusions. This is explained by the large damping parameter γ assumed in the calculation, reflecting the poor conductivity of MnP and an electronic mean free path on the order of the nanoparticles' size.

The MO response of our heterogeneous samples is more realistically modeled with ellipsoidal inclusions oriented in all directions with respect to the applied field and gyrotropic axis. Figures 2(a) and 2(b) show the calculated absorption and

rotation spectra for a fixed population of prolate revolution ellipsoids having a long semiaxis 1.5 times longer than the small axes (eccentricity of 0.745). In this configuration, allowing the ellipsoids to orient randomly, the spectral lines associated with the individual eigenvalues of the depolarization factor are noticeable, in spite of the large damping parameter. Again, a higher filling factor of MnP lowers the resonance energy. Figures 2(c) and 2(d) show the absorption and rotation spectra for the more general case of an ensemble of ellipsoids with constant distribution of eccentricities: revolution ellipsoids having their singular semiaxis a_x ranging from $a_x = 0.3a_y$ to $a_x = 5a_y$, with $a_y = a_z$, implying eccentricities ranging from 0 to 3.18 for oblate ellipsoids and from 0 to 0.97 for prolate ellipsoids. The frequency dependent absorption lines associated with individual depolarization factor eigenvalues are merged into a single broad resonance in the absorption spectrum. Absorption maxima are at 1.56 and 1.53 eV, for $f = 3.8\%$ and 13.7%, respectively. In contrast, two peaks can clearly be identified in the rotation spectra. The peak at lower energy corresponds to the resonance for spherical inclusions, while the one at higher energy coincides with the maximum in absorption for the ensemble of randomly oriented ellipsoids of various shapes.

The combination of positive rotation at the resonance energy and negative rotations below and above resonance, for all inclusions, leads to a two-peak feature in the rotation which is not seen in absorption spectra. In both rotation and absorption spectra of randomly oriented ellipsoids with constant distribution of shapes, the higher energy resonance that appears originates from the large number of nanoclusters with high eccentricities, for which the variations in eccentricities lead to relatively small shift in the population-specific resonance energy. Thus, randomly oriented inclusions characterized by a uniform eccentricity distribution exhibit a resonance at higher energy compared to spherical inclusions.

One further modification of the model to properly account for real materials is to consider an effective inverse relaxation time in the form $\gamma \rightarrow \gamma_{\text{eff}} = \gamma + J\omega^2$. Many authors have introduced this modification to the relaxation time to describe the behavior of various metals in the infrared and visible part of the EM spectrum, where the Drude invariant relaxation time cannot adequately explain observed permittivities.[19,20] Adding this phenomenological damping term to the intrinsic permittivity dampens the negative wing of the rotation line shape at higher energy (see Fig. 2) and fuses both peaks into a broad effective resonance. This additional term will allow a better fit to the experimental data presented in Sec. VI.

In summary, a model describing the GaP:MnP effective medium based on Maxwell-Garnett mixing rules indicates that allowing inclusions of various shapes and orientations dampens the diagonal effective permittivity resonance responsible for absorption, as it has been pointed out in the literature on surface plasmon resonance.[21,22] Also, a mixture of differently shaped ellipsoidal inclusions with random orientation gives rise to magneto-optical activity spectra showing more features than the corresponding absorption spectra. Since rotation spectra are less likely than absorption spectra to lose their features due to a distribution in the shapes and orientations of the inclusions, it is an advantageous tool to investigate effective media.
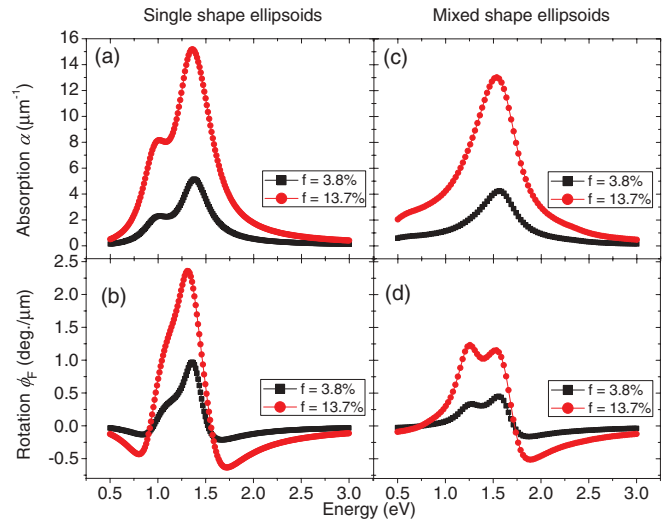

FIG. 2. (Color online) (a) Absorption and (b) rotation spectra calculated from the effective permittivity components for a randomly oriented single population of prolate revolution ellipsoids with an eccentricity fixed at 0.745. (c) Absorption and (d) rotation spectra calculated from effective permittivity components for randomly oriented revolution ellipsoids having a constant distribution of eccentricities ranging from 0 to 0.97 for prolates and 0 to 3.18 for oblates. All spectra feature inclusion volume fractions of 3.8% and 13.7%. The maxima in absorption and rotation are still functions of the volume fraction. For all rotation spectra, the internal effective magnetic field was set at $\lambda M = 15$ T.

IV. MAGNETO-OPTICAL APPARATUS AND MEASUREMENT TECHNIQUE

To investigate the magneto-optical properties of the MnP thin film and the GaP:MnP epilayers as a function of the sample temperature, radiation wavelength, and applied dc magnetic field, the custom-built setup whose schematics is shown in Fig. 3 was used. This system includes a supercontinuum laser source (L) providing probe wavelengths ranging from 400 nm to 1 μm (1.25 to 3.1 eV), which can be replaced by several lasers operating at 630, 655, and 830 nm (not shown). The supercontinuum was spectrally filtered with a volume Bragg grating (F) providing a bandpass of 2 nm. The polarization was controlled with two Glan-Taylor prisms (P, A) and an achromatic quarter-wave plate (QW). The temperature of the sample, inside a cryostat (C), could be varied from 11 K to 325 K. The sample holder was designed to allow light to go through the sample at normal incidence (henceforth referred to
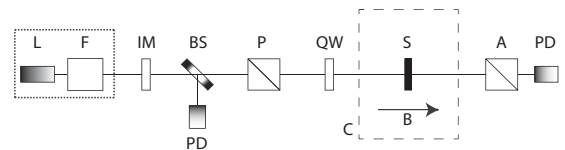

FIG. 3. Schematics of the experimental setup used to investigate the MO properties as a function of wavelength and polarization of the incident radiation, sample temperature, and DC applied magnetic field. The various elements are described in the text. The dashed source box including the supercontinuum laser and tunable filter can be exchanged for lasers emitting at 630, 655, and 830 nm.

as the measurement axis), parallel to the dc magnetic field (B). In this Faraday configuration, field values up to ±410 mT could be applied. The detection apparatus consisted of an optical chopper (IM) and two sets of silicon photodiodes (PD), preamplifiers, and lock-in amplifiers. Great care was taken to correctly characterize the temperature and maintain it constant throughout the measurement since the magnetization of MnP around room temperature varies strongly, and a corresponding large effect on the MO spectra were expected. Note that the quarter-wave plate shown (QW) is not used for Faraday rotation measurements.

The Faraday rotation (θ_F), in degrees, induced by the magnetization of the sample was quantified as follows. The angular position of the analyzer corresponding to extinction was determined from a parabolic fit of the transmitted intensity as a function of analyzer angle. This allowed us to determine the exact rotation angles corresponding to both applied magnetic field extrema (±410 mT). Rotating the analyzer by 45° from the extinction condition at $H_0 = 0$, the measured transmitted intensity is then directly proportional, for small angles, to the rotation angle induced by the magnetization. For all Faraday hysteresis curves to be shown here, the field was swept from −410 to +410 mT and back.

The MCD was measured by removing the analyzer (A) from the setup shown in Fig. 3 and by adding a quarter-wave plate (QW) to generate right and left circularly polarized light incident on the sample. The dichroism, given as the angle ξ_F, is defined in Sec. VI and depends on the variation of the transmitted intensity of circularly polarized light as a function of the applied magnetic field.

V. MAGNETIZATION AND ORIGIN OF MAGNETO-OPTICAL ACTIVITY

The Faraday rotation being proportional to sample thickness, the contribution from substrates was important for all samples studied. However, due to their linear response with magnetic field, these relatively larger contributions could easily be accounted for and reliably subtracted. For the glass substrate, the measured rotation per unit length followed the tabulated value of 0.24°/(T·mm) at 300 K and slightly decreased at lower temperatures, as expected from the positive dn/dT coefficient in the Becquerel formula.[23] For GaP substrates, a value of 11.5°/(T·mm) was found at 655 nm and 300 K, also decreasing as a function of temperature and increasing with photon energy. The rotation was found to be independent of the crystal orientation and was attributed to free carriers. For all data presented and discussed hereafter, contributions from substrates were subtracted.

Faraday rotation is first presented as a function of temperature and applied magnetic field perpendicular to the sample plane using a probe energy of 1.89 eV for the 2 μm thick GaP:MnP epilayer. Figures 4(a) and 4(b) present the rotation (θ_F) and magnetization curve (M/M_S) for sample B4 at 210, 270, and 287 K. The magnetization measurements were made using a vibrating sample magnetometer (VSM). Here, M_S is the saturation magnetization measured at 2.2 T and 210 K. Similar results were obtained for all samples. The close match between magnetization and rotation presented in these figures provides strong evidence that the origin of
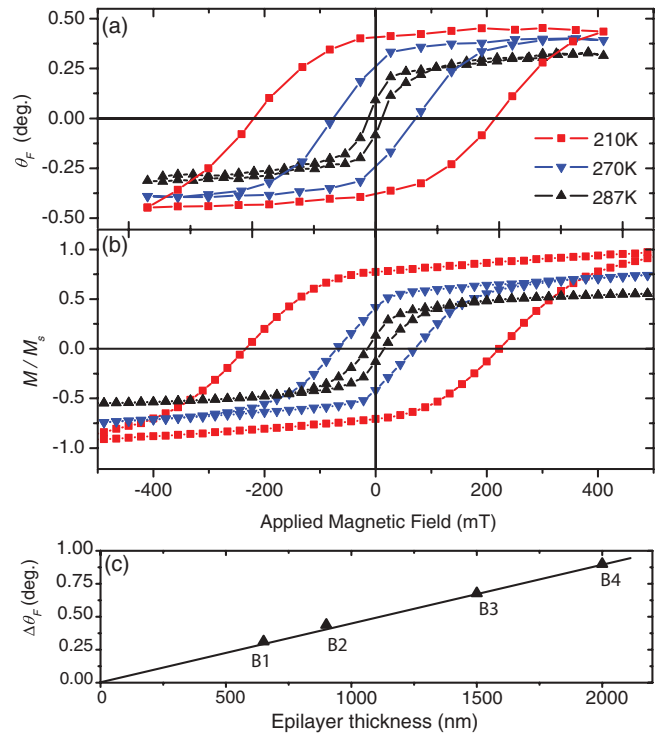

FIG. 4. (Color online) (a) Faraday rotation of sample B4 versus applied magnetic field for several temperatures (red square 210 K, blue down triangle 270 K, black up triangle 287 K) with the substrate contribution subtracted. The probing energy is 1.89 eV. (b) VSM measurements of the same sample at the same temperatures. The M_s value is taken at 2.2 T and 210 K. (c) Linear dependence of total Faraday rotation [$\Delta\theta_F = \theta_F(410\,\text{mT}) - \theta_F(-410\,\text{mT})$] as a function of thickness for B1, B2, B3, and B4 measured at 210 K and 1.89 eV.

Faraday rotation is directly related to the ferromagnetic state of the nanoclusters. As expected, the total rotation $\Delta\theta_F = \theta_F(410\,\text{mT}) - \theta_F(-410\,\text{mT})$ is also directly proportional to the thickness for the four samples from set B, as shown in Fig. 4(c).

Figure 5 compares the Faraday rotations of samples A1, B4, and C1 at 210 K. The rotations were normalized by the sample thickness and MnP volume concentration to obtain units of degrees per mm of MnP, ($\phi_F = \theta_F/l_{\text{MnP}}$). Samples B4 and C1 both show a rotation per equivalent amount of MnP that is larger than that of the MnP film A1, with B4 having almost twice the rotation per thickness of MnP than that of A1 at fields of ±410 mT. The inset of Fig. 5 shows that the Faraday rotation per mm produced by the GaP substrate at 210 K and 1.89 eV is very weak compared to that of the MnP containing layers.

The differences between the shapes of the magnetization hysteresis curve for samples A1, B4, and C1 reflect the different effective magnetic anisotropy in the out-of-plane direction. For a monodomain spherical inclusion, with uniaxial anisotropy, the M_r/M_S ratio is 0 if the field is aligned along a hard axis and 1 if it is instead aligned along an easy axis. For a randomly oriented ensemble of nanoclusters, this ratio is 0.5. The experimentally measured ratios using VSM hysteresis curves at 210 K are, for samples A1, B4, and C1, 0.26, 0.77, and 0.37, respectively. These differences are in agreement with the respective orientations of the magnetic easy axis with respect
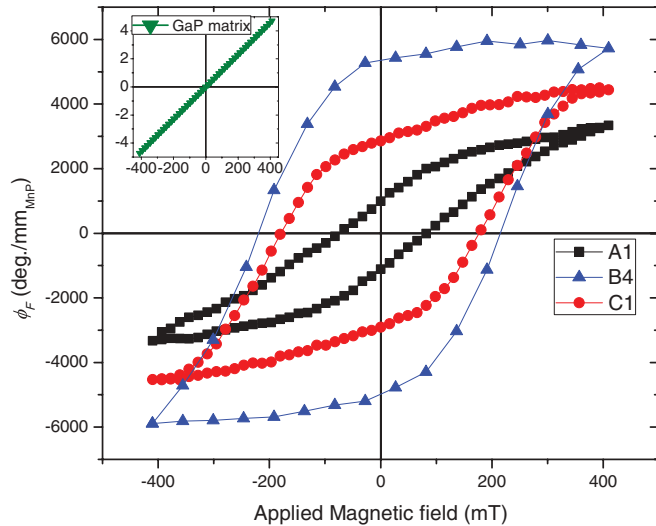
FIG. 5. (Color online) Faraday rotations ϕ_F in samples A1, B4, and C1 per thickness of MnP versus applied magnetic field at 210 K and 1.89 eV. The normalization process allows us to visualize the distinct enhancement of the rotation for MnP in cluster form compared to the film. The inset shows the rotation induced in a GaP matrix of the same thickness for the same fields and temperature. Clearly, the GaP:MnP systems have higher magneto-optical activity than the sum of their constituents.

to the measurement axis for all heterogeneous samples, as supported by the XRD and FMR data for preferred orientations of MnP presented in Refs. 12 and 24.

While the VSM configuration measured the out-of-plane component of the magnetization (same axis as the applied magnetic field and optical measurement axis for MO experiments), the induced polarization rotations are expected to be also sensitive to in-plane magnetizations. However, in-plane magnetization effects were neglected as they are proportional to the square of the in-plane magnetization components, which should be small at the magnitude of perpendicularly applied magnetic fields. Furthermore, for polycrystalline sample A1 where the magnetic easy plane is isotropic, and for samples B and C1, for which the average in-plane projection of all easy axes cancels out, the net in-plane magnetization upon field reversal is expected to be negligible. Therefore, the MO hysteresis curves obtained did not manifest any antisymmetric signature and the Faraday rotation amplitudes are expected to depend linearly on the out-of-plane magnetization induced by the magnetic field.

The dependence of the Faraday rotation on the magnetization can be empirically described by the relation $\theta_F = K\mu_0 M l_{MnP}$, where K is an empirical magneto-optical coupling parameter, $\mu_0 M$ is the MnP phase magnetization (in teslas), and l_{MnP} is the effective MnP thickness of the sample. K must not be confused with the effective internal coupling

constant (λ) defined in Sec. III. The magneto-optical coupling parameters K are calculated as an average from the measured rotation and magnetization as a function of magnetic field and are presented in Table II. While the correspondence of the magnetization and rotation curves was nearly perfect for samples B1–B4 (see Fig. 4), slight differences between the magnetic and MO hysteresis curves could be observed for samples A1 and C1 (not shown). This aspect is reflected in the uncertainty on the values of K in Table II. It is interesting to note that the values for GaP:MnP are very similar for all B and C1 samples, and significantly higher than that of the MnP metallic layer. If the MnP magnetization had been the sole source of induced rotation, the same value should have been obtained from these samples. We thus conclude that this enhancement for GaP:MnP samples originates from a magnetoplasmonic resonance of the effective medium, as will be further demonstrated below.

A useful metric for comparing magneto-optical activity from different materials is the Verdet constant expressed as $\theta_F = V B_0 l$, where l is the material thickness. For our hysteretic magnetic materials, we calculated this Verdet constant for different temperatures from the linear slope of θ_F at coercivity, for both the real thickness l (corresponding to V) and the effective thickness l_{MnP} (corresponding to V_{MnP}). The results are presented in Table III for the MnP film A1, epilayers B4 and C1, and the substrates of glass and GaP for comparison. While similar to the above described phenomenological optical activity based on magnetization, this form depends on the applied induction field $B_0 = \mu_0 H_0$ and does not explicitly incorporate the magnetization field. In our samples, however, the magnetization contribution to the effective induction field is much more important than the applied magnetic field, so it is important to note that the values for the Verdet constants given in Table III, while in $°\cdot$(T mm)$^{-1}$ to follow the general convention in the literature, only reflect the response to the applied magnetic induction field. This form has the advantage of comparing the rotary power of a material based on a fully controlled parameter: the applied magnetic field. For example, at coercivity, the rotation slopes at a temperature of 287 K and an energy of 1.89 eV are $1.14°$/T for A1, $7.10°$/T for B4, and $4.94°$/T for C1. Normalizing by the overall MnP volume present in the sample that contributes to the optical activity, epilayers B4 and C1 induce larger rotations than the A1 MnP film by factors ranging from 2 to 8, depending on the temperature, as indicated by the values of V_{MnP} in Table III. Since the Verdet constant per effective MnP length is evaluated at coercivity, higher value for samples B1–B4 are observed compared to C1 because of the effective anisotropy resulting from the projection of MnP nanoclusters' easy axes on the measurement axis. This is not the case for K values presented in Table II, where results were made independent of magnetic anisotropy by independently measuring the magnetization. The uncertainty for all values

TABLE II. Magneto-optical coupling constants at incident photon energy of 1.89 eV.

	A1	B1	B2	B3	B4	C1
K [$°$/(mT $\cdot$ μm)]	12.5 ± 0.4	15.2 ± 0.2	15.5 ± 0.2	15.4 ± 0.2	15.3 ± 0.2	15.1 ± 0.4

TABLE III. Rotation slope and Verdet constants measured at coercivity for an incident radiation of 1.89 eV.

	Temperature (K)	A1	B4	C1	GaP	Glass
Rotation [$°\cdot$T^{-1}]	210	1.45	3.61	3.38		
	270	1.37	3.77	4.3		
	287	1.14	7.1	4.94		
V [$°\cdot$(T mm)$^{-1}$]	210	14500	1805	4072	9.39	0.23
	270	13700	1885	5181	10.1	0.24
	287	11400	3550	5952	11.4	0.24
V_{MnP} [$°\cdot$(T mm)$^{-1}$]	210	14500	47500	29725		
	270	13700	49605	37816		
	287	11400	93421	43444		

presented in Table III is approximately 5% to 10%. They were evaluated from the variance of multiple measurements of the rotation as a function of applied magnetic field at both the positive and negative coercivity fields.

It is clear that the magneto-optical activity in terms of Faraday rotation in the GaP:MnP and MnP films originates from the magnetization of the ferromagnetic metallic phase of MnP, as the shape of the MO hysteresis curves matching closely the results obtained by VSM. We point out that the optical system probing the MO activity is sensitive enough to reproduce and characterize the magnetic anisotropies of this type of sample.

VI. SPECTRAL DEPENDENCE OF THE MAGNETO-OPTICAL ACTIVITY

The spectral dependence of the Faraday rotation was studied in the visible portion of the electromagnetic spectrum for all samples listed in Table I. The measured total Faraday rotation $\Delta\theta_F = \theta_F(410 \text{ mT}) - \theta_F(-410 \text{ mT})$ for the MnP film sample A1 at 290 and 210 K is shown in Fig. 6. As expected from the temperature dependence of the magnetization and optical activity presented in Sec. V, the rotation decreases at higher temperatures. The monotonic increase of the rotation as a function of energy and its saturation above 2 eV are similar at both temperatures. As expected, no spectral features could be identified. The effective medium model derived in Sec. III does not apply to a uniform metallic film: To accurately model spectral dependence of the magneto-optical activity of an MnP thin film, an explicit angular frequency dependence of the effective MO coupling parameter $[\lambda(\omega)M]$ would be required in Eq. (A2), which falls outside the scope of this paper.

In contrast to the case of the MnP thin film, the total rotation $\Delta\theta_F$ as a function of photon energy from samples with embedded MnP clusters (B and C) exhibits a broad resonance, as shown in Fig. 7 for B4. For this sample and all others from set B, a maximum is observed at 1.70 eV. Indeed, for all temperatures below T_C, the magneto-optical rotation increases with energy, reaches a maximum, and then drops rather abruptly. The spectral position of the maximum does not vary as the sample temperature is varied, but the amplitude of the rotation resonance rapidly decreases with increasing temperature. The maximum in the rotation spectrum is attributed to resonant magneto-optical activity of nonspherical MnP nanoclusters randomly embedded in a high dielectric constant semiconductor.
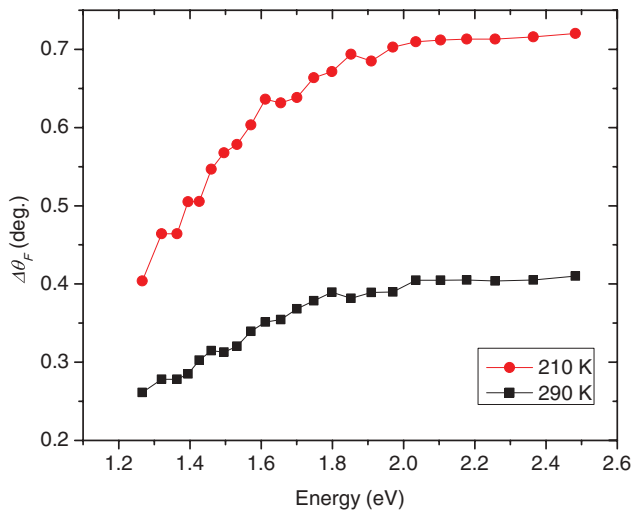

FIG. 6. (Color online) Total Faraday rotation $\Delta\theta_F = \theta_F(410 \text{ mT}) - \theta_F(-410 \text{ mT})$ for sample A1 at 210 K and 290 K. The rotation increases with incident photon energy and saturates around 2 eV.
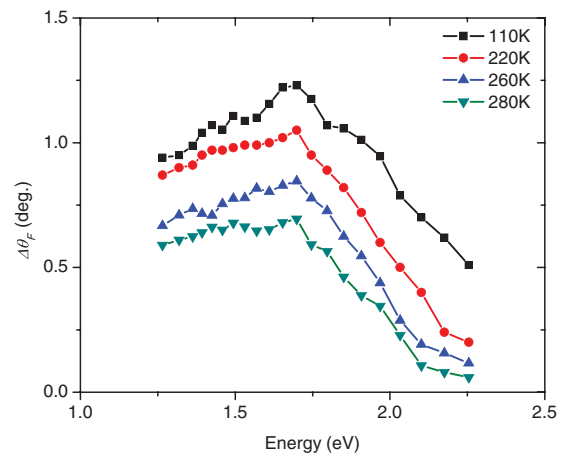

FIG. 7. (Color online) Faraday rotation $\Delta\theta_F = \theta_F(410 \text{ mT}) - \theta_F(-410 \text{ mT})$ for sample B4 as a function of incident photon energy. The spectral maximum in rotation is located at 1.70 eV and is independent of temperature. In contrast to sample A1, the MO activity reaches a maximum and then abruptly drops.
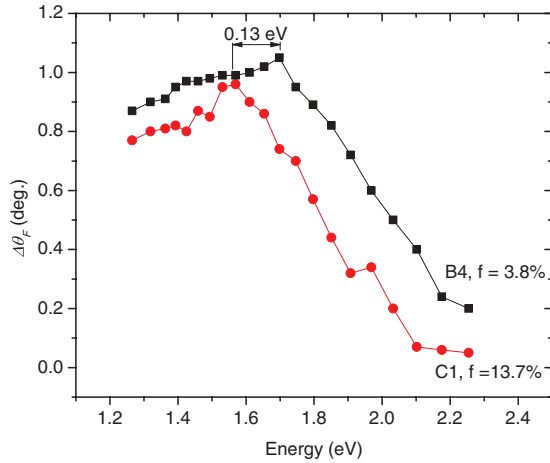
FIG. 8. (Color online) Total Faraday rotation $\Delta\theta_F = \theta_F(410\,\text{mT}) - \theta_F(-410\,\text{mT})$ as a function of incident photon energy for samples B4 and C1 at 210 K. The spectral maximum in rotation shifts from 1.70 eV to 1.57 eV with an increase of the volume fraction of MnP from 3.8% to 13.7%.

Figure 8 compares the total Faraday rotation spectra of samples B4 and C1 at a temperature of 210 K. While the spectral line shape is similar for both samples, the resonance of C1 occurs at a lower energy of 1.57 eV. This shift of 0.13 eV is explained by the dependence of the resonant plasmonic frequency on the filling factor of the MnP nanoclusters in the epilayer as exemplified in Sec. III.

Figure 9 shows the theoretical total Faraday rotations for samples B4 and C1 using the effective inverse relaxation time $\gamma \to \gamma_{\text{eff}} = \gamma + J\omega^2$ presented in Sec. III and their respective parameters. The effective MO coupling parameter field is $\lambda M = 15$ T and the contribution from the applied field was
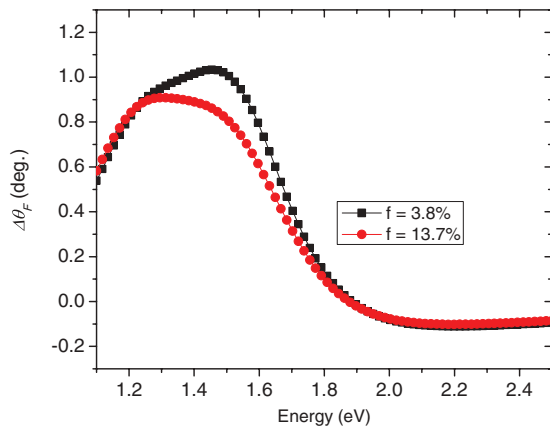

FIG. 9. (Color online) Calculated total Faraday rotation $\Delta\theta_F = \theta_F(410\,\text{mT}) - \theta_F(-410\,\text{mT})$ as a function of incident photon energy for the parameters of samples B4 ($f = 3.8\%$) and C1 ($f = 13.7\%$). This calculation accounts for random nanocluster orientations, constant distribution of shape factors, and a frequency dependent relaxation parameter γ_{eff}. The spectral maximum in rotation shifts from 1.46 eV to 1.28 eV with an increased volume fraction of MnP from 3.8% to 13.7%. The effective internal magnetic field λM is set at 15 T. For sample C1, a normalization factor was applied to account for the difference in $M(H)$ measured with VSM at 210 K when compared to B4.

negligible in this simulation. The amplitudes of rotation are seen to be comparable to the measured quantities for those two samples. The maximum rotation calculated energy for samples B4 and C1 is 1.46 eV and 1.28 eV, respectively. The energy shift (0.18 eV) as a function of the filling factor is comparable to the energy difference measured experimentally (0.13 eV).

The calculated effective medium resonance energy is about 0.25 eV lower than the measured spectral maximum in total rotation angle $\Delta\theta_F(\omega = \omega_{\text{max}})$. It is important to note that in this Maxwell-Garnett approach, a constant real permittivity for the GaP host across the investigated spectrum was used and that the MO coupling relies solely on the conduction electrons modeled with a Drude permittivity with enhanced coupling to the magnetization state of MnP through an effective magnetic field included in the form λM. With these considerations in mind, it is not surprising that the resonant frequencies do not match more closely. Nonetheless, it is clear that the host semiconductor explains the appearance of a resonant frequency for MO effects shifted to the near infrared. In addition, the model successfully explains the redshift of the resonance with the increase in the volume fraction of inclusions. Therefore, we infer that the resonant behavior observed in Fig. 7 and Fig. 8 is a magnetoplasmonic enhancement of the Faraday rotation.

The influence of the host dielectric permittivity on the magnetoplasmonic resonance energy is further demonstrated by sample D1 consisting of MnP nanoclusters embedded in polystyrene. As shown in Fig. 10, the low dielectric constant of this host (2.51 vs 11 for GaP, at 1.9 eV) produces a well-defined resonance in Faraday rotation at 2.90 eV rather than at 1.70 eV for sample B4. Just like for samples B4 and C1, the use of Drude's model in the effective medium approach discussed in Sec. III underestimates the resonance energy, but it clearly corroborates the magnetoplasmonic resonance origin of this optical effect. Also, the effect of the shape and orientation distribution on the broadening of the line shape is limited in Ps:MnP by having nearly spherical inclusion. Comparing
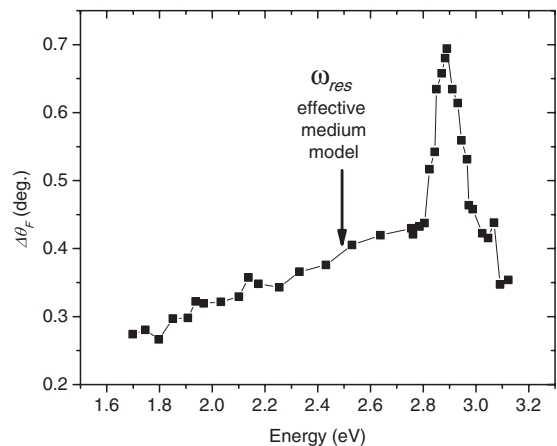

FIG. 10. Total Faraday rotation $\Delta\theta_F = \theta_F(410\,\text{mT}) - \theta_F(-410\,\text{mT})$ as a function of incident photon energy for sample D1 at 230 K. The resonance is located at 2.90 eV. The polystyrene matrix has a much lower dielectric constant and therefore shifts the resonance of the effective medium to higher energy compared to the GaP matrix. Our effective medium model predicts the resonance at 2.44 eV.
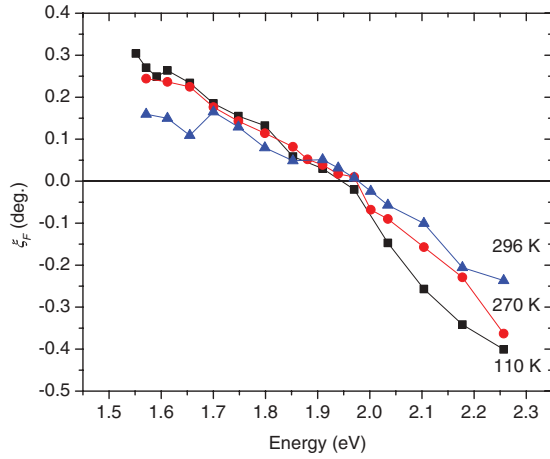
FIG. 11. (Color online) Spectral magnetocircular dichroism ξ_F for sample B4 at 110, 270, and 296 K for an applied field magnitude of ± 410 mT. The MCD angle starts positive at lower energy and crosses zero at around 1.95 eV for all temperatures.

Fig. 10 with Fig. 8, the resonance of Ps:MnP is significantly narrower than that of GaP:MnP. While samples B1–B4 and C1 exhibit a relatively narrow size distribution and a large eccentricity distribution, the opposite is true for sample D1. We have thus verified that the variation in eccentricity determines the magnetoplasmonic resonance linewidth.

The Faraday rotation angle per unit length, Eq. (4), includes the actual rotation of the polarization plane (real part), and the MCD (imaginary part): $\Phi_F = \phi_F + i\chi_F$. To further investigate the magnetoplasmonic origin of the magneto-optical properties of these samples, we measured the MCD spectra, expecting the resonant behavior of $\theta_F = \phi_F l$ to be associated with a zero-MCD crossing in χ_F. It is measured experimentally as $\text{MCD}_H = (T_+ - T_-)/(T_+ + T_-)$ for a given value of field H, where T_+ and T_- denote the transmitted intensity of right and left polarized light, respectively. The MCD angle ξ_F, expressed in degrees, is then defined as $\xi_F = \chi_F l = 180(\text{MCD}_{H+} + \text{MCD}_{H-})/(2\pi)$. For all measurements presented below, ξ_F was measured at fields $H = \pm 410$ mT.

Figure 11 shows ξ_F as a function of photon energy for sample B4 measured at three temperatures and Fig. 12 compares ξ_F measured for samples B4 and C1 at 287 K. As for the MnP film (A1), ξ_F does not vary significantly in the investigated spectral window (not shown); it remains constant at about 0.3°. In contrast, the angle measured from samples B4 and C1 varies considerably: It is positive at low energy, decreases monotonically as a function of energy, and then crosses to negative angles. The zero crossing $\xi_{F,0}$ is at 1.95 eV for sample B4 and all type B samples (not shown) and 1.85 eV for C1. Although the shift of 100 meV is somewhat smaller than the one obtained from the Faraday rotation spectra shown in Fig. 8, it is again explained by a shift of the magneto-plasmonic resonance as a function of the MnP volume fraction. Using the effective medium model for effective permittivities, the MCD evaluated from $\xi_F = \text{Im}[\frac{\omega\sqrt{\mu_0}}{2}\frac{\epsilon_{\text{eff},t}}{\sqrt{\epsilon_{\text{eff},\perp}}}]l$ is plotted in Fig. 13 for $f = 3.8\%$ and 13.7%. The crossovers are seen to appear at a somewhat lower energy than the corresponding maxima in θ_F, but reproduce
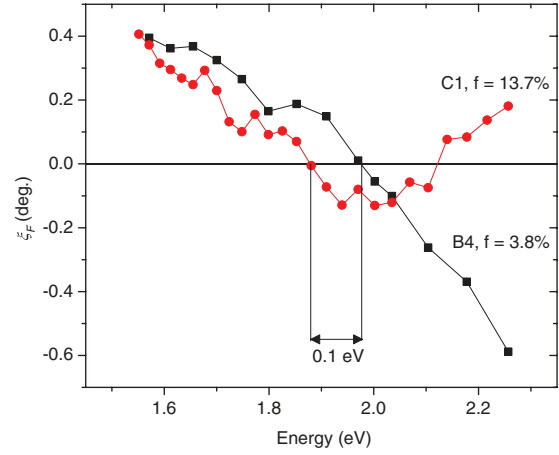

FIG. 12. (Color online) Spectral magnetocircular dichroism ξ_F for samples B4 and C1 at 287 K for an applied field magnitude of ± 410 mT. The MCD angle starts positive at lower energy for both epilayers and it crosses zero at a lower energy (0.1 eV) for C1. While the MCD for B4 keeps decreasing towards the semiconductor gap, it undergoes another crossover for C1 and is again positive at the GaP energy gap of 2.27 eV at 287K.

the low-energy zero MCD of Fig. 12 and the volume fraction dependent energy shift (0.06 eV in place of 0.1 eV).

Although those zero-MCD points were expected to occur at the same energy as the rotation maxima, there is an energy difference of 0.35 eV between $\theta_{F,\text{max}}$ and $\xi_{F,0}$ for both samples. This shift might originate from the fact that the semiconductor absorption near the band gap induces a large variation in the effective permittivity tensor element responsible for the dichroism, and has not been taken into account in this effective medium model (constant permittivity host).

The MCD measurements thus also support the argument for a magnetoplasmonic enhancement of MO properties in nanocluster systems since varying the MnP concentration shifts the first crossover point $\xi_{F,0}$. Furthermore, the absolute reduction of the amplitude of the MCD with increasing temperature reinforces the role played by the magnetization
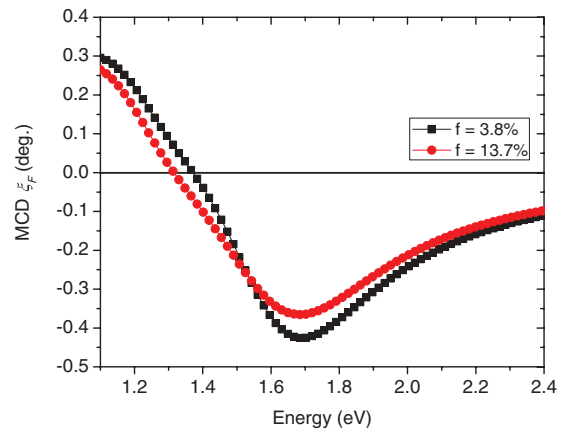

FIG. 13. (Color online) Calculated magnetocircular dichroism ξ_F as a function of energy for the equivalent parameters of samples B4 ($f = 3.8\%$) and C1 ($f = 13.7\%$). The zero-MCD point shifts from 1.37 to 1.31 eV when increasing the volume fraction of MnP from 3.8% to 13.7%. The effective field is set at $\lambda M = 15$ T.

on the imaginary part of the off-diagonal tensor element of the effective permittivity.

Finally, although the effective medium model cannot predict the exact position of the magnetoplasmonic resonance, it qualitatively explains important features of these experimental results. A more rigorous model taking into account the spectral dependence of the permittivity, both of the ferromagnetic metal and of the semiconductor, would be necessary to precisely analyze the energy of the observed resonances.

VII. DISCUSSION

The parallel electron energy-loss spectroscopy measurements in samples from set B grown by MOVPE[11] show no evidence of a GaMnP phase. However, this method is not sensitive enough to probe small concentrations ($\leqslant 0.5\%$) of substitutional and intersticial Mn in GaP. In the case of sample C1 where the MnP concentration is very high, a dilute GaMnP phase may be present. In this case, two additional mechanisms other than the magnetoplasmonic resonance can be expected to contribute to the near gap MCD.[25] First, there is the giant Zeeman splitting, which is widely used to interpret the sign of MCD at the semiconductor gap in II-Mn-VI diluted magnetic semiconductors. Second, varying degrees of Mn impurity level compensation in the gap can lead to a reversed sign of MCD at the band gap energy. In the first mechanism, the sign of MCD at the band gap indicates the type of magnetic coupling (FM or AFM) for the *p-d* exchange constant β of the assumed GaMnP phase. The impact of this mechanism is larger for temperatures below the Curie temperature of the dilute phase, but can nonetheless affect the MCD above the Curie temperature. Near the band gap, the splitting between circularly-right and -left polarized photon absorption transitions is reflected on the MCD spectrum. In the second mechanism, a higher concentration of Mn forming a dilute GaMnP phase and impurity bands can lead to sign reversal of MCD when compared to normal Zeeman splitting. In our case, those mechanisms could lead to the offset of 0.35 meV between the zero-MCD points and the maximum Faraday rotations measured, as well as explain why the sign of MCD near the gap energy is opposite in B4 and C1 with another crossover observed near 2.13 eV for sample C1, containing a much higher Mn concentration.

Mn pnictides (MnX compounds, with $X =$ P, As, Sb, Bi), with their strong spin-orbit coupling, are known for their favorable MO properties.[26] Results presented here confirm that this is also the case for the less studied MnP. GaP:MnP offers a number of attractive advantages with respect to the very similar GaAs:MnAs. First, the former has a higher energy gap for optical applications in both the infrared and the visible regions of the spectrum. Second, the lattice constant of GaP is similar to that of Si, making it a prime candidate for epitaxial growth of integrated optoelectronic devices. Most interestingly, the Faraday rotation per unit thickness measured at a temperature of 289 K under an external field of 200 mT of GaP:MnP exceeds that of GaAs:MnAs[27] by a factor of two despite operating almost at the MnP Curie temperature. The normalized rotation induced by MnP nanoclusters appears to be larger than that of MnAs over an important region of the spectrum. Finally, this stronger MO activity is not hindered by increased absorption, as the measured transmission losses for both systems are comparable in the investigated photon energy range.

Transmission losses for light below the GaP band gap originate from absorption and scattering from MnP inclusions. Considering the nanoclusters' size, only the former is dominant in our systems. A plasmonic resonance should be accompanied by a large absorption in the diagonal elements of the permittivity tensor. However, absorption measurements performed in the same spectral window did not show a significant increase in absorption in the vicinity of the MO activity resonance for samples of set B and for C1. Instead, a monotonic increase in absorption is observed approaching the semiconductor gap. We explain the absence of well defined absorption features associated with the magnetoplasmonic resonance by the presence of extrinsic effects significantly broadening the absorption spectrum. As discussed in Sec. II, the MnP nanoparticles have a relatively important distribution of diameters and eccentricities. The latter have been shown to severely broaden the plasmonic absorption line shape, while inhomogeneous effects dampen the plasmonic magneto-optical response features to a lesser extent (see Sec. III). Furthermore, MnP being a poor conductivity metal compared to Ag and Au, a considerable broadening of absorption spectra would be expected even for narrow nanocluster eccentricity distribution.[21,22]

The intensity absorption coefficient 2α (from Beer-Lambert law $I = I_0 e^{-2\alpha L}$) at 1.89 eV is about 12.96 μm^{-1} for A1, 1.19 μm^{-1} for samples B1–B4, and 2.77 μm^{-1} for C1. Although the rotation per unit thickness is somewhat comparable in all samples, absorption is considerably more important in the MnP film. Normalizing the Verdet constant at coercivity to the absorption losses to obtain a figure of merit in $°/(dB \cdot T)$, we evaluate the effective rotations of samples A1, B1–B4, and C1 to be 0.23, 0.38, and $0.44°/(dB·T)$ at 270 K, respectively. Compared to the uniform MnP thin film, the nanocluster systems are advantageous by factors of 1.5 to 2, due to the enhanced MO activity from the energy-shifted plasmonic resonance, and nonproportional increase in losses for those photon energies.

As demonstrated above, plasmonic effects in GaP:MnP enhance the magneto-optic response with respect to simple MnP films. However, the figure of merit remains lower than what is needed for optoelectronic applications which should amount to about $45°/(dB·T)$. To enhance all magneto-optical properties, it is essential to optimize the size uniformity and gain a better control of the shape distribution of the nanoclusters.

VIII. CONCLUSION

The amplitude of the Faraday rotation as a function of applied field closely matches the hysteresis observed in magnetization measurements made by VSM. The experimental setup used to investigate the MO properties of MnP thin film and GaP:MnP epilayers proved to be sensitive enough to reproduce effective magnetization anisotropy. The match between both types of hysteresis confirmed the linear dependence on magnetization of the measured Faraday rotations. Compared to a uniform MnP film, the amplitude of the induced rotations per unit of magnetization in MnP nanocluster systems is enhanced by a factor of 20%, the net rotation per unit thickness of MnP is two times higher, and, at coercivity, rotations per units of applied field can be 8 times larger. The spectral dependence of the Faraday rotation and the magnetocircular dichroism shows

qualitative agreement with the effective medium model for magnetoplasmonic resonance, assuming an effective internal magnetic field proportional to the magnetization. The variation of MnP nanocluster concentration in the epilayers reproduced the spectral shift in the effective resonance frequency, as predicted by the effective medium model. The mismatch between the spectral position of the maximum rotation and zero MCD is not surprising since the model does not take into account the full complexity of the MnP permittivity spectrum, the host permittivity spectrum, and the additional semiconductor near gap effects on its optical properties. Instead, the magneto-optical activity is simply described by the electron cyclotron frequency, which is enhanced by spin-orbit coupling. The model has nonetheless the merit of describing the main features of the magnetoplasmonic resonance effect.

The MO activity in MnP was found to be large in all samples, but the absorption measurements indicate that the samples investigated so far are not quite fit for direct integration into optical devices. The figure of merit of our samples is still too low compared to required rotation to losses ratio. However, magnetoplasmonic MnP nanocluster systems do increase the figure of merit by a factor of 2 at resonance when compared to MnP film. A more uniform nanocluster shape distribution and size in the fabrication process would lead to reduced broadening in the MO resonance and allow for deeper analysis of the plasmonic and magneto-optical coupling.

APPENDIX A: EFFECTIVE PERMITTIVITY TENSOR

The dielectric permittivity of a degenerate electron gas can be derived from Drude's frequency dependent conductivity in the form $\sigma(\omega) = \frac{\sigma_0}{1 - i\omega\tau}$, where $\sigma_0 = \frac{n_e e^2 \tau}{m^*}$ is the dc conductivity, τ is the relaxation time, n_e is the electron density, e is the electron charge, and m^* the electron effective mass. Considering an effective internal magnetic field parallel to the light propagation vector, including the applied field ($\vec{H} = H_0 \hat{z}$) and a term in the form λM, the permittivity takes the form

$$\overleftrightarrow{\epsilon_i} = \begin{pmatrix} \epsilon_\perp & -i\epsilon_t & 0 \\ i\epsilon_t & \epsilon_\perp & 0 \\ 0 & 0 & \epsilon_\parallel \end{pmatrix}, \tag{A1}$$

where

$$\epsilon_t = \frac{-\epsilon_0 \omega \omega_c \omega_p^2}{(\omega^2 + i\omega\gamma)^2 - (\omega\omega_c)^2},$$

$$\epsilon_\perp = \epsilon_\infty - \frac{\epsilon_0 \omega_p^2 (\omega^2 + i\omega\gamma)}{(\omega^2 + i\omega\gamma)^2 - (\omega\omega_c)^2}, \tag{A2}$$

$$\epsilon_\parallel = \epsilon_\infty - \frac{\epsilon_0 \omega_p^2}{(\omega^2 + i\omega\gamma)}.$$

The parameters in these equations are defined in Sec. III. This form implicitly assumes that the magnetization of the medium is parallel to the applied magnetic field. Strong magnetocrystalline anisotropy and texture in the magnetic axis orientations for MnP nanoclusters in the GaP matrix for samples from set B and C mean that rigorous treatment of the $\vec{B}(\vec{H}, \vec{M})$ relation for a single nanocluster would lead to a gyrotropic tensorial permittivity without the symmetry of Eq. (A1), and no zero components. However, in a normal-incidence geometry and in the first-order Faraday rotation regime, only linear terms in magnetization (and field) from the $\overleftrightarrow{\epsilon_i}_{12} = -\overleftrightarrow{\epsilon_i}_{21}$ components will contribute to the optical activity. Moreover, in-plane components of the magnetization ($\perp$ to $\hat{z}$) of a large ensemble of inclusions are expected to cancel each other, leaving only a negligible second-order magnetization contribution to optical activity from terms not included in our definition of ϵ_t. We therefore proceed in our analysis with the simplified permittivity described by Eq. (A1) and (A2).

The characteristic angular frequencies for the permittivity terms in Eq. (A2) follow the relation $\omega_p \gg \omega_c$ for ferromagnetic metals with effective Weiss-like induction field value as high as 1000 T. At optical frequencies where $\omega_p > \omega > \omega_c$, and the very high frequency permittivity parameter ϵ_∞ can be taken as ϵ_0, the permittivity tensor elements of the metallic inclusions can be reduced to $\epsilon_\perp = \epsilon_\parallel = \epsilon_0 - \frac{\epsilon_0 \omega_p^2}{(\omega^2 + i\omega\gamma)}$ and $\epsilon_t = \frac{-\epsilon_0 \omega \omega_c \omega_p^2}{(\omega^2 + i\omega\gamma)^2}$; therefore Eq. (A1) reduces to Eq. (1) in the text.

APPENDIX B: EFFECTIVE MEDIUM PERMITTIVITY

Generalizing the effective permittivity of a Maxwell-Garnett effective medium quickly becomes cumbersome when gyrotropy is induced by an applied magnetic field and the inclusions are allowed various shapes and orientations with respect to the applied field. The constitutive relation is used to determine the effective permittivity tensor,

$$\overleftrightarrow{\epsilon}_{\text{eff}} \cdot \langle \vec{E} \rangle = \epsilon_m \langle \vec{E} \rangle + \langle \vec{P} \rangle, \tag{B1}$$

where the averaged polarization,

$$\langle \vec{P} \rangle = \left[\overleftrightarrow{I} - \frac{n_i \overleftrightarrow{\alpha_i}}{\epsilon_m} \cdot \overleftrightarrow{N_i} \right]^{-1} \cdot n_i \overleftrightarrow{\alpha_i} \cdot \langle \vec{E} \rangle, \tag{B2}$$

is in turn defined by the number density of inclusions n_i, the shape factor depolarization tensor of the inclusion population ellipsoids $\overleftrightarrow{N_i}$, and their polarizability

$$\overleftrightarrow{\alpha_i} = V(\overleftrightarrow{\epsilon_i} - \epsilon_m \overleftrightarrow{I}) \cdot [\epsilon_m \overleftrightarrow{I} + \overleftrightarrow{N_i} \cdot (\overleftrightarrow{\epsilon_i} - \epsilon_m \overleftrightarrow{I})]^{-1}, \tag{B3}$$

with V being the volume of inclusions and $\overleftrightarrow{I}$ the identity tensor. Equation (B3) is valid for a specific population of inclusions sharing the same ellipsoidal shape and orientation angle Ω with respect to the applied magnetic field. To account for various inclusion populations with a distribution of shapes and orientations, a weight function ρ_k must be added to correctly model an ensemble of individual populations with specific polarizability $\overleftrightarrow{\alpha_k}$. This polarizability is then a function of the specific orientation Ω and depolarization tensor $\overleftrightarrow{N_k}$.[28,29]

The MnP nanoclusters' ellipsoids have textured orientations in the GaP matrix, mostly following the magnetocrystalline orientation distribution. The large number of directions present for the inclusion populations allows for a uniform distribution in orientation in a first approximation. Thus, assuming randomly oriented inclusions, each of constant volume V but with varying shapes, the polarizability is then expressed as

$$\overleftrightarrow{\alpha_i} = \sum_k \rho_k \int_\Omega d\Omega \overleftrightarrow{\alpha_k}(\Omega) = V \sum_k \rho_k \int_\Omega d\Omega(\overleftrightarrow{\epsilon_i} - \epsilon_m \overleftrightarrow{I}) \cdot [\epsilon_m \overleftrightarrow{I} + \overleftrightarrow{N_k}(\Omega) \cdot (\overleftrightarrow{\epsilon_i} - \epsilon_m \overleftrightarrow{I})]^{-1}. \tag{B4}$$

Inserting this polarizabilty (B4) in expression (B2), the effective permittivity of the medium (B1) is obtained [Eq. (2)]. The different tensor elements must be computed numerically for the general case at hand. They do have simple analytic form for simpler cases such as spherical inclusions, or if the ellipsoids all have the same shape factor and all have the same main ellipsoidal axis pointing in the gyrotropic axis defined by the applied magnetic field.

---

*sebastien.francoeur@polymtl.ca

[1] I. Mayergoyz, Physica B **407**, 1307 (2011).

[2] W. Brullot, V. Valev, and T. Verbiest, Nanomedicine (Philadelphia) **8**, 559 (2012).

[3] S. M. S M Hamidi, M. M. Tehranchi, and S. Sadeghi, J. Phys. D **44**, 305003 (2011).

[4] L. Wang, C. Clavero, Z. Huba, K. J. Carroll, E. E. Carpenter, D. Gu, and R. A. Lukaszew, Nano Lett. **11**, 1237 (2011).

[5] V. I. Safarov, V. A. Kosobukin, C. Hermann, G. Lampel, J. Peretti, and C. Marlière, Phys. Rev. Lett. **73**, 3584 (1994).

[6] C. Hermann, V. A. Kosobukin, G. Lampel, J. Peretti, V. I. Safarov, and P. Bertrand, Phys. Rev. B **64**, 235422 (2001).

[7] C.-M. Wei, C.-W. Chen, C.-H. Wang, J.-Y. Chen, Y.-C. Chen, and Y.-F. Chen, Opt. Lett. **36**, 514 (2011).

[8] A. A. Zharov and V. V. Kurina, J. Appl. Phys. **102**, 123514 (2007).

[9] G. Monette, C. Lacroix, S. Lambert-Milot, V. Boucher, D. Menard, and S. Francoeur, J. Appl. Phys. **107**, 09A949 (2010).

[10] R. A. Booth, M. Marinescu, J. Liu, and S. A. Majetich, J. Magn. Magn. Mater. **322**, 2571 (2010).

[11] S. Lambert-Milot, C. Lacroix, D. Menard, R. A. Masut, P. Desjardins, M. Garcia-Hernandez, and A. de Andres, J. Appl. Phys. **104**, 083501 (2008).

[12] C. Lacroix, S. Lambert-Milot, P. Desjardins, R. A. Masut, and D. Menard, J. Appl. Phys. **105**, 07C119 (2009).

[13] A. De Andres, A. Espinosa, C. Prieto, M. Garcia-Hernandez, R. Ramirez-Jimenez, S. Lambert-Milot, and R. A. Masut, J. Appl. Phys. **109**, 113910 (2011).

[14] E. Huber and D. H. Ridgley, Phys. Rev. **135**, A1033 (1964).

[15] E. Palik and J. Furdyna, Rep. Prog. Phys. **33**, 1193 (1970).

[16] G. R. Fowles, *Introduction to Modern Optics* (Dover, 1975).

[17] J. Choi, S. Choi, M. Sohn, H. Park, Y. Park, H. Park, S. Hong, and S. Cho, J. Magn. Magn. Mater. **304**, 112 (2006).

[18] H. Akinaga, M. Mizuguchia, T. Managoa, E. Gan'shinab, A. Granovskyb, I. Rodinb, A. Vinogradovb, and A. Yurasovb, J. Magn. Magn. Mater. **242-245**, 470 (2002).

[19] J. B. Smith and H. Ehrenreich, Phys. Rev. B **25**, 923 (1982).

[20] F. Parmigiani, E. Kay, T. C. Huang, J. Perrin, M. Jurich, and J. D. Swalen, Phys. Rev. B **33**, 879 (1986).

[21] D. D. Nolte, J. Appl. Phys. **76**, 3740 (1994).

[22] D. Crouse, D. D. Nolte, J. Chang, and M. R. Melloch, J. Appl. Phys. **81**, 7981 (1997).

[23] P. Williams, A. H. Rose, G. W. Day, T. E. Milner, and M. N. Deeter, Appl. Optics **30**, 1176 (1991).

[24] C. Lacroix, S. Lambert-Milot, P. Desjardins, R. A. Masut, and D. Menard, J. Appl. Phys. **103**, 07D531 (2008).

[25] M. Berciu, R. Charkavorty, Y. Y. Zhou, M. T. Alam, K. Traudt, R. Jakiela, A. Barcz, T. Wojtowicz, X. Lui, J. K. Furdyna, *et al.* , Phys. Rev. Lett. **102**, 247202 (2009).

[26] M. Coey, *Magnetism and Magnetic Materials* (Cambridge University Press, 2010).

[27] H. Akinaga, S. Miyanishi, K. Tanaka, W. Van Roy, and K. Onodera, Appl. Phys. Lett. **76**, 143302 (2000).

[28] A. H. Sihvola and J. A. Kong, IEEE T. Geosci. Remote **26**, 420 (1988).

[29] A. H. Sihvola, *Electromagnetic mixing formulas and applications* (The Institution of Electrical Engineers, 1999).